Journal of Zhejiang University-SCIENCE B (Biomedicine & Biotechnology) in press
www.jzus.zju.edu.cn; www.springer.com/journal/11585
E-mail: jzus_b@zju.edu.cn

Research Article

https://doi.org/10.1631/jzus.B2300679

Single-cell and spatial transcriptomic analysis reveals that an immune cell-related signature could predict clinical outcomes for microsatellite stable colorectal cancer patients receiving immunotherapy

Shijin YUAN[1,2], Yan XIA[1,3], Guangwei DAI[1,3], Shun RAO[1,3], Rongrong HU[1,3,4], Yuzhen GAO[1,3], Qing QIU[1,3], Chenghao WU[1,3], Sai QIAO[1,3], Yinghua XU[2], Xinyou XIE[1,3], Haizhou LOU[2], Xian WANG[2]✉, Jun ZHANG[1,3]✉

[1]*Department of Clinical Laboratory, Sir Run Run Shaw Hospital, Zhejiang University School of Medicine, Hangzhou, 310016, Zhejiang, China*
[2]*Department of Medical Oncology, Sir Run Run Shaw Hospital, Zhejiang University School of Medicine, Hangzhou, 310016, Zhejiang, China*
[3]*Key Laboratory of Precision Medicine in Diagnosis and Monitoring Research of Zhejiang Province, Hangzhou, 310016, Zhejiang, China.*
[4]*Yongkang Hospital of Traditional Chinese Medicine Medical Community Xicheng Branch, Jinhua, 321300, Zhejiang, China*

Abstract: Recent data suggest that vascular endothelial growth factor receptor inhibitor (VEGFRi) could enhance the anti-tumor activity of the anti-PD-1 antibody in colorectal cancer (CRC) with microsatellite stability (MSS). However, the comparison between this combination and standard third-line VEGFRi treatment is not established and reliable biomarkers are still lacking. We retrospectively enrolled MSS CRC patients receiving anti-PD-1 antibody plus VEGFRi (combination group, n=54) or VEGFRi alone (VEGFRi group, n=32), and their efficacy and safety were evaluated. We additionally examined the immune characteristics of the MSS CRC tumor microenvironment (TME) through single-cell and spatial transcriptomic data, and an MSS CRC immune cell-related signature (MCICRS) predicting the clinical outcomes of MSS CRC patients receiving immunotherapy was developed and validated in our in-house cohort. Compared to VEGFRi alone, anti-PD-1 antibody and VEGFRi combination exhibited a prolonged survival benefit (median progression-free survival: 4.4 vs. 2.0 months, P=0.0024; median overall survival: 10.2 vs. 5.2 months, P=0.0038) and similar adverse events incidence. Through single-cell and spatial transcriptomic analyses, we determined 10 MSS CRC-enriched immune cell types and their spatial distribution, including naïve CD4T, regulatory CD4T, Th17, exhausted CD8T, cytotoxic CD8T, proliferated CD8T, NK, plasma, and classical and intermediated monocytes. Based on a systemic meta-analysis and 10 machine learning algorithms, we obtained MCICRS, an independent risk factor for the prognosis of MSS CRC patients. Further analyses demonstrated that the low-MCICRS group presented a higher immune cell infiltration and immune-related pathway activation, and hence a significant relation with the superior efficacy of pan-cancer immunotherapy. More importantly, the predictive value of MCICRS in MSS CRC receiving immunotherapy was also validated with the in-house cohort. Anti-PD-1 antibody combined with VEGFRi presented an improved clinical benefit in MSS CRC with manageable toxicity. MCICRS could serve as a robust and promising tool with which to predict clinical outcomes for individual MSS CRC patients receiving immunotherapy.

Key words: Colorectal cancer; Microsatellite stable; Immunotherapy; Single-cell RNA sequencing; Spatial transcriptomics

1 Introduction

Colorectal cancer (CRC) ranks among all cancer types as the third highest in terms of incidence and second highest in terms of mortality worldwide (Sung et al., 2021). In China, CRC is the one of five most commonly

✉ Jun ZHANG, jameszhang2000@zju.edu.cn
Xian WANG, wangx118@zju.edu.cn
Jun ZHANG, https://orcid.org/0000-0002-2613-3165

Received Sept. 21, 2023; Revision accepted Jan. 25, 2024;
Crosschecked xxx. xx, 20xx; Published online xxx. xx, 20xx

diagnosed cancer and is the leading cause of cancer related death in both genders, with around 408,000 new cases and 195,600 deaths in 2016 (Zheng et al., 2023). For locally advanced or metastatic CRC, chemotherapy based on 5-fluorouracil is the standard first- and second-line treatment, including FOLFOX (5-fluorouracil, leucovorin plus oxaliplatin) and FOLFIRI (5-fluorouracil, leucovorin plus irinotecan) alone or combined with vascular endothelial growth factor (VEGF) blocker bevacizumab or epidermal growth factor receptor blocker cetuximab (if RAS wild-type) (Modest et al., 2019). Two small-molecule inhibitors that target the VEGF receptor (VEGFR)—regorafenib and fruquintinib—have been approved to treat patients progressed after chemotherapy in China. Although regorafenib or fruquintinib presented an improved survival compared with placebo, less than 5% of patients achieved an objective response, indicating that the clinical benefit of the VEGFR inhibitor (VEGFRi) is still limited, and exploring other effective treatment strategies for chemotherapy-refractory CRC patients remains an unmet need (Grothey et al., 2013; Li et al., 2018).

Recently, immunotherapy represented by immune checkpoint inhibitors (ICIs), such as anti-cytotoxic T-lymphocyte antigen 4 (CTLA4) antibody ipilimumab and anti-program death-1 (PD-1) antibodies pembrolizumab and nivolumab, have exhibited durable anti-tumor activity in various cancers, which revolutionized the field of cancer treatment. Notably, single agent or doublet ICIs have reached 30–60% of the objective response rate (ORR) in a handful CRC patients who are characterized as microsatellite instability-high (MSI-H), a molecular phenotype of CRC that is due to mismatch repair-related gene mutation (Le et al., 2015; Le et al., 2017; Overman et al., 2017; Overman et al., 2018; Andre et al., 2020; Le et al., 2020). Based on these results, pembrolizumab or nivolumab monotherapy, and nivolumab combined with ipilimumab, have been approved for the treatment of MSI-H CRC. However, immunotherapy is particularly ineffective in patients with microsatellite-stable (MSS), a population that comprises about 85% of advanced CRC. The treatment failure is primarily due to the immunosuppressive tumor microenvironment (TME) of MSS CRC. Hence, the combination of ICIs and other therapies to reverse the immune suppressive environment may be the key to treating MSS CRC.

The mechanisms of VEGF-mediated immune suppression have been widely clarified. Blocking the VEGF-related pathway could normalize vascular construction, inhibit immunosuppressive cells production—such as regulatory T cells (Tregs) and myeloid-derived suppressor cells (MDSC)—and increase effector T cells infiltration in the TME (Rahma and Hodi, 2019). Therefore, it is reasonable to consider that VEGFRi has a synergistic effect with immunotherapy through restoring immune activity in MSS tumors. Three current single-arm clinical trials showed that ICIs combined with VEGFRi have an inspiring anti-tumor activity in MSS CRC (Fukuoka et al., 2020; Cousin et al., 2021; Kim et al., 2022), whereas a comparison between this combination and standard third-line treatment is still lacking. Meanwhile, identifying predictive biomarkers to select suitable patients to receive immunotherapy is critically important. Single-cell RNA sequencing (scRNA-seq) and spatial transcriptomic data provide the comprehensive characteristics of TME cell-type composition, distribution, and heterogeneity, which help to advance our understanding of key features of tumorigenesis, metastasis, and drug resistance.

In this work, we evaluate the efficacy and safety of anti-PD-1 antibody and VEGFRi combination compared with VEGFRi alone in MSS CRC. Through scRNA-seq and spatial transcriptomic data, we determine the MSS CRC-enriched immune cells' gene signature and assess its predictive value for the prognosis, recurrence, and benefits of immunotherapy in MSS CRC. Our work may help optimize precision treatment and further improve the clinical outcomes of CRC patients.

2 Materials and Methods

2.1 Study design, patient enrollment, data collection, and treatment procedure

This study retrospectively evaluated the efficacy and safety of anti-PD-1 antibody and VEGFRi combination therapy compared to VEGFRi monotherapy in MSS CRC, and was approved by the Ethics Committee of Sir Run Run Shaw Hospital (certificate no. 20190211-55); the project was carried out in accordance with the Helsinki Declaration.

Eligible patients were pathologically confirmed to have unresectable locally advanced or metastatic MSS CRC, and the progression of previous chemotherapy. The exclusive criteria were as follows: (1) autoimmune disease history or any underlying immune dysfunction disease; (2) an Eastern Cooperative Oncology Group performance status (ECOG PS) of 3 or higher; (3) inadequate bone marrow hematopoietic, hepatic, and renal function. Patients receiving anti-PD-1 antibody and VEGFRi (regorafenib or fruquintinib) were enrolled as the combination group, while patients receiving VEGFRi monotherapy were enrolled as the VEGFRi group. All enrolled participants signed an informed consent form. Baseline clinical characteristics of each enrolled patient were collected from electronic medical records. Peripheral blood lymphocyte and monocyte counts of each patient were obtained within 1 week before treatment initiation through the Hematology Analyzer System (Beckman Coulter LH780 ANl6104).

With regards to treatment procedure, in the VEGFRi group, patients received regorafenib or fruquintinib orally once daily for 3 weeks and were off treatment for 1 week in a 4-week cycle. In the combination group, anti-PD-1 antibody was given intravenously starting on day 1 of VEGFRi initiation.

2.2 Therapeutic efficacy, survival, and safety assessment

Therapeutic efficacy was evaluated by radiologists and investigators every 6 weeks after treatment initiation according to the Response Evaluation Criteria in Solid Tumors version 1.1, and was documented as complete response (CR), partial response (PR), stable disease (SD), and progressive disease (PD). ORR was defined as the percentage of patients with CR or PR, and DCR was defined as the percentage of patients with CR, PR, or SD. PFS was defined as the duration from the date of treatment initiation to disease progression or death due to any cause, whichever occurred first. OS was defined as the duration from the date of treatment initiation to death due to any cause. All treatment-related adverse events (AEs) were evaluated and graded according to the Common Terminology Criteria for Adverse Events version 4.0.

2.3 Public scRNA-seq, spatial transcriptomic, and bulk RNA-seq data collection

The scRNA-seq data of CRC were collected from two independent datasets including GSE132465 and GSE146771 (Lee et al., 2020; Zhang et al., 2020). Specifically, GSE132465 contained 65,362 single cells from 23 CRC patients (4 MSI and 19 MSS) of 33 samples (23 tumor and 10 adjacent normal tissues); and GSE146771 contained 54,285 single cells from 18 CRC patients (3 MSI and 15 MSS) of tumors, adjacent normal tissue, and blood samples. All CRC patients were treatment-naïve and all single cells underwent quality control for further analyses. The spatial transcriptomics (ST) data of CRC patients were downloaded from the website (http://www.cancerdiversity.asia/scCRLM/) of a spatial transcriptomics study including 8 samples from 4 patients (Wu et al., 2022). Four paired primary and liver metastatic tumor samples from 2 treatment-naïve patients, named CRC-P1, LM-P1, CRC-P2, and LM-P2, were used for spatial analyses. In addition, a total of 1293 MSS CRC patients with bulk RNA-seq data from 7 public datasets were accessed from The Cancer Genome Atlas (TCGA) and Gene Expression Omnibus (GEO). Among these, the TCGA-CRC cohort was composed of 418 patients from TCGA-COAD and -READ datasets, and the GEO-meta cohort was composed of six datasets including GSE39582 (n=459), GSE39084 (n=54), GSE41258 (n=137), GSE92921(n=53), GSE143985 (n=85), and GSE30378 (n=87). Furthermore, 23 pan-cancer immunotherapy cohorts with therapeutic efficacy, prognosis, and bulk RNA-seq data were also collected, including 1 MSS CRC dataset, 12 melanoma datasets, 2 lung cancer datasets, 2 renal carcinoma datasets, 2 urothelium carcinoma datasets, 1 breast cancer dataset, 1 gastric cancer dataset, 1 hepatocellular carcinoma dataset, and 1 esophagus cancer dataset. The detailed information about each dataset is presented in Table S4.

2.4 scRNA-seq data processing and analysis

The scRNA-seq data analysis was performed using the "Seurat" R package. First, the batch effects among different samples were corrected using the canonical correlation analysis method (Butler et al., 2018). Then, the top 2000 highly variable genes were identified by the "FindVariableFeatures" function for further principal component analysis (PCA) and t-distributed stochastic neighbor embedding (t-SNE) dimensionality reduction. Further, we used the "FindClusters" function to obtain different cell clusters, and the "FindAllMarkers" function to determine the differentially expressed genes (DEGs) for each cluster. Lastly, we annotated different cell types manually according to the well-known marker genes and previous research.

2.5 Tissue distribution preference analysis

To characterize the tissue distribution of different cell types, we calculated odds ratios (ORs) to indicate preferences through Fisher's exact test. An OR value > 1.5 indicated that cell type was preferentially distributed in tissue, whereas an OR value < 0.5 indicated that cell type preferred not to be distributed in tissue (Zheng et al., 2021).

2.6 Cell–cell communication analysis

Based on a ligand–receptor interaction database, the cell–cell communication network was analyzed using the "CellChat" R package to explore the communication probability of different cell subtypes, major pathway signaling, and ligand–receptor pairs (Jin et al., 2021). The "netVisual_circle" function was used to visualize the interaction numbers and strength among different cell subtypes.

2.7 Pseudotime trajectory analysis

The "monocle" R package was performed to illustrate the cell state transition of different cell types including CD4T+ cells, CD8+T cells, and monocytes; a reversed graph embedding technique was applied to reconstruct single-cell trajectories (Qiu et al., 2017). Briefly, highly variable genes were identified for semi-supervised trajectory reconstruction. Dimensional reduction and cell ordering were performed using the DDRTree method and the "orderCells" function. The "plot_cell_trajectory" function was used to visualize the dynamic pseudotime trajectories of different cell types.

2.8 Spatial transcriptomic data processing and cell type identification

The spatial transcriptomic data of each sample were processed using the "Seurat" R package and were analyzed separately. In detail, data were normalized using the "SCTransform" method, and were then submitted to perform "RunPCA", "FindNeighbors", and "FindClusters" to obtain clusters of spatial spots with similar transcriptomic characteristics. In consideration of the fact that each spot contained about 10 cells, we could not identify the certain cell type for each spot. Hence, using cell type annotation information from scRNA-seq data as a reference, combined with pathological feature of H&E staining section, we predict the main cell types of spatial spots using the "FindTransferAnchors" and "TransferData" functions of "Seurat". As for immune cell subtypes annotation, based on DEGs and the well-known marker genes of each cell subtype, we used a signature-based strategy to score each cell subtype enrichment via the "AddModuleScore" function, which was visualized by the "SpatialFeaturePlot" function.

2.9 Bulk RNA-seq data processing

The RNA-seq raw read counts data of the TCGA-CRC cohort were downloaded via the "TCGAbiolinks" R package, and were further converted to transcripts per kilobase million (TPM) value and were log-2 transformed (Colaprico et al., 2016). For the microarray data of 6 GSE CRC cohorts, we used the normalized matrix files downloaded from the GEO database.

In addition, among 23 immunotherapy cohorts, the RNA-seq data of the IMvigor210 cohort were available from the "IMvigor210" R package (Mariathasan et al., 2018). The expression data of other cohorts were downloaded from the GEO database or supplementary files from corresponding research.

2.10 Weighted correlation network analysis (WGCNA)

Co-expression gene networks of the TCGA-CRC cohort were generated via the "WGCNA" R package (Langfelder and Horvath, 2008). An appropriate soft threshold β was calculated for the scale-free network. The weighted adjacency matrix was converted into a topological overlap matrix (TOM), and the corresponding dissimilarity was generated (1-TOM). The dynamic tree cutting approach was used to identify different modules. The module that displayed the highest correlation with immune cell enrichment was chosen for further analysis, and the genes with both high gene significance (GS) and module membership (MM) were defined as immune cell-related hub genes.

2.11 MSS CRC immune cell-related signature generated from machine learning-based integrative approaches

To develop a stable and accurate MSS CRC immune cell-related signature (MCICRS), we first used a

multivariable Cox proportional hazards regression analysis to obtain OS-related genes in TCGA-CRC, GSE39582, and GSE41258 cohorts adjusting by age, gender, and TNM stage. Through the "meta" R package, the hazard ratio (HR) of each OS-related gene was pooled in the random-effects model of a systematic meta-analysis, and the stable prognostic genes were determined. Then, we integrated 10 machine learning algorithms, including random survival forest (RSF, "randomForestSRC" R package), Lasso ("glmnet" R package), elastic network (Enet, "glmnet" R package), Ridge ("glmnet" R package), stepwise Cox ("survival" R package), CoxBoost ("CoxBoost" R package), partial least squares regression for Cox (plsRcox, "plsRcox" R package), supervised principal components (SuperPC, "superpc" R package), generalized boosted regression modelling (GBM, "superpc" R package), and survival support vector machine (survival-SVM , "survivalsvm" R package), and a total of 96 algorithm combinations to fit prediction models across TCGA-CRC, GSE39582, GSE39084, and GSE41258 cohorts. The concordance index (C-index) was calculated for each model, and the model with the highest average C-index was considered optimal.

2.12 Immune infiltration analysis

A total of 7 algorithms, including single-sample gene set enrichment analysis (ssGSEA, "GSVA" R package), xCell ("xCell" R package), ESTIMATE ("esitimate" R package), quanTIseq ("immunedeconv" R package), MCP-counter ("MCPcounter" R package), EPIC ("EPIC" R package), and the TIMER database were employed to quantify the relative infiltration abundance of different TME immune cell types in the TCGA-CRC cohort.

Furthermore, the gene set variation analysis (GSVA, "GSVA" R package) and gene set enrichment analysis (GSEA, "clusterProfiler" R package) were performed to investigate the activity of pathway signaling based on hallmark gene sets (h.all.v7.5.1.symbols, MSigDB database, http://www.gsea-msigdb.org/gsea/msigdb/).

2.13 Proteomic analysis through proteomaps

We used proteomaps to analyze and visualize the composition of protein abundances and their functions (https://bionic-vis.biologie.unigreifswald.de/) (Liebermeister et al., 2014). The proteomaps could be divided into six different functional parts, including "genetic information processing", "metabolism", "organismal systems", "environmental information processing", "human disease", and "cellular processes". Each protein was shown as a polygon-shaped tile with an area representing protein abundance, and functional-related proteins appeared in adjacent regions.

2.14 Statistical analysis

Categorical variables were reported as frequencies and percentages, and their significance was compared using the Chi square test. For continuous variables, student's t-test or Wilcoxon test were used for comparison between two groups, and one-way ANOVA or the Kruskal–Wallis test for comparison among three groups. In addition, Pearson's correlation test was used for assessing correlations between two continuous variables.

The best cut-off value was determined by the "survminer" R package. The Kaplan–Meier method and log-rank test were used for survival analysis via the "survival" R package. Multivariable Cox regression analysis was used to identify significant prognostic variables and calculated HR and 95% confidence interval (95% CI), visualized using the "forestplot" R package. The nomogram was developed using the "rms" R package and the time-dependent area under the receiver operating characteristic curve (ROC) curve (AUC) was evaluated using the "timeROC" R package. All statistical analyses were performed using the R software version 4.0. All statistical tests were two-tailed and a P-value less than 0.05 was considered statistically significant.

3 Results

3.1 The immune and angiogenic landscape in the MSS CRC tumor microenvironment

The overall design of this study is displayed in Figure 1A. To better elucidate the TME cellular composition of a CRC tumor, we analyzed a total of 65,362 cells from scRNA-seq data, and 8 major cell types were annotated (Figure S1A and Figure S2A-B). Therein, the MSS tumor had the highest proportion of epithelial cells and the lowest immune cells infiltration compared to the MSI tumor and adjacent normal tissue (Figure

S2C). In order to illustrate the effect of immune suppression and angiogenesis in MSS CRC tumors, we first investigated the immune checkpoint and VEGF pathway-related genes expression among different cell types (Figure S1B). Compared to adjacent normal tissue, we observed a high expression of majority immune checkpoint genes in T cells from the MSS tumor, such as PDCD1 (PD-1), CD274 (PD-L1), CTLA4, LAG3, TIGIT, and HAVCR2 (TIM-3), indicating an exhausted state of T cells in the TME. In addition, VEGFA and VEGFB were highly expressed in malignant epithelial and myeloid cells and fibroblasts in tumor tissue, demonstrating that these cell types were the main sources of angiogenic factor release. In addition, we found high co-expression of CD274, HAVCR2, VEGFA, and FLT1 (VEGFR1) in tumor myeloid cells, suggesting their critical role in maintaining a suppressed immune and pro-angiogenic TME.

Due to the complexity of intratumor architecture, we next explored the immune checkpoint and VEGF pathway-related genes' spatially expressed location in ST data (Figure S1C). We found a highly spatial co-expression of CD68, ENG, and PECAM1, indicating a wide distribution of myeloid cells in the stromal region. Meanwhile, VEGFA and VEGFB were also co-expressed in the same area, which was consistent with the scRNA-seq data. Interestingly, there was a subset of exhausted CD8+T cells (high expression of CD3D, CD8A, PDCD1, CTLA4, and TIGIT), co-localized VEGFB+ myeloid cells wrapped around endothelial cells, indicating a physical interaction of VEGF-driven angiogenesis and immune suppression. Additionally, a significant positive correlation was observed between the immune checkpoint and VEGF-related angiogenic signatures among all spots of ST data (Figure S1D). Furthermore, in MSS CRC tumors, the extensive communications among malignant epithelial, myeloid, and endothelial cells and fibroblasts through the VEGF signaling pathway were presented by the cell-chat analysis (Figure S1E-F). Collectively, these findings verified the synergistic effect between immunosuppression and angiogenesis from single-cell and spatial dimensions, and hinted that the combination of immunotherapy and anti-angiogenic therapy might enhance anti-tumor activity in MSS CRC.

3.2 Immunotherapy combined with anti-angiogenic therapy improved the clinical outcomes of MSS CRC patients

In order to evaluate the efficacy and safety of immunotherapy combined with anti-angiogenic therapy in MSS CRC, we retrospectively enrolled 54 patients receiving anti-PD-1 antibody plus VEGFRi combination as a combination group. For comparison, 32 patients receiving standard VEGFRi monotherapy were enrolled as a VEGFRi group. The baseline clinical characteristics of patients between the two groups were basically balanced (Table S1). At the cutoff date, the median follow-up time was 5.8 (IQR 3.1-10.7) months in the combination group and 3.8 (IQR 2.0-6.4) months in the VEGFRi group (Table S2). PR was observed in two patients in the combination group (ORR: 3.7%) but in no patients in the VEGFRi group (ORR: 0%). The DCR of the combination group was significantly higher than that of the VEGFRi group (66.7% vs. 28.1%, P = 0.0012, Figure 1B). For the survival comparison between the two groups, the combination group showed a longer median PFS (4.4 vs. 2.0 months, P= 0.0024, Figure 1C) and OS (10.2 vs. 5.2 months, P= 0.0038, Figure 1D). Considering the differentiation of targets between fruquintinib and regorafenib, we compared the outcomes of anti-PD-1 antibody plus fruquintinib, anti-PD-1 antibody plus regorafenib, and the VEGFRi group separately, and we found that the treatment response and survival between the anti-PD-1 antibody plus fruquintinib, and anti-PD-1 antibody plus regorafenib groups was comparable, while both were superior to those of the VEGFRi group, verifying the reliability of our results (Figure S3A-C). In addition, the subgroup analyses revealed an improved survival benefit for anti-PD-1 antibody plus VEGFRi combination therapy when patients were stratified into majority subgroups based on different clinical characteristics, such as age $\geqslant$ 54, being male, an ECOG of 1, the right side of the primary tumor, $\leqslant$ 2 metastatic sites and lung metastasis (Figure 1E-F).

Treatment-related AEs of any grade were reported equally between the two groups, including 52 patients (96.3%) in the combination group and 30 patients (93.8%) in the VEGFRi group (P > 0.99, Table S3). Therein, grade 3 AEs were reported in 16 patients (29.6%) in the combination group and 8 patients (25%) in the VEGFRi group, respectively (P = 0.91). The most common AEs in two groups were fatigue (32 [50%] in the combination group and 15 [46.9%] in the VEGFRi group) and proteinuria (25 [46.3%] in the combination group and 12 [37.5%] in the VEGFRi group, Figure 1G). In addition, a total of 6 patients in the combination group (9.4%) experienced immune-related AEs including pneumonia, myocarditis, and thyroiditis, and all patients resumed treatment after AEs solved. Overall, the above results demonstrated that immunotherapy combined with anti-angiogenic therapy exhibited a robust anti-tumor activity and improved the clinical outcomes of MSS CRC

patients with manageable toxicity. Hence, we further investigated the particular TME immune characteristics of MSS CRC patients and identified the potential subsets suitable for immunotherapy.

3.3 A single-cell transcriptomic atlas in the MSS CRC tumor immune microenvironment

Since immune cells were major effectors in immunotherapy, we first re-clustered lymphocytes (T/B/plasma cells) in scRNA-seq data and identified 14 cell subtypes (Figure 2A, S2D and Table S5). Based on cell proportion and tissue distribution preference analyses, the naïve CD4T, CD4Treg, CD4Th17, exhausted CD8T, cytotoxic CD8T, proliferated CD8T, NK, and IgG plasma cells showed a strong distribution preference in MSS tumors (Figure 2B-C and Table S6). In addition, cell-chat analysis revealed that naïve CD4T, exhausted CD8T, and epithelial cells had more communications with other cells in MSS tumors (Figure 2D). We next explored the dynamic immune states and cell transitions in MSS CRC-infiltrated CD4+T and CD8+T cells by inferring the state trajectories. The pseudotime analysis showed that naïve CD4T cells were at the beginning of the trajectory path, whereas several CD4Th17 cells and most CD4Treg cells were at a terminal state (Figure 2E). Similarly, we also found that the proliferated CD8T cells primarily aggregated on the initiation of the pseudotime trajectory, and exhausted CD8T and cytotoxic CD8T cells were located in different directions (Figure 2F). The trajectory information indicated the different functional divergence of T cells in the MSS tumor; accurately identifying the MSS subtype with activated immune and transcriptional states may help to expand the immunotherapy candidates.

Similarly, we re-clustered myeloid cells and identified 9 cell subtypes, of which classical monocytes and intermediated monocytes were considered MSS tumor-enriched cell subtypes (Figure 2G-I, S2E and Table S7-8). Additionally, a wider crosstalk between monocytes and other cells was observed in MSS tumors through cell-chat analysis (Figure 2J). Furthermore, the pseudotime trajectory displayed a distinct distribution of monocyte subclusters (Figure 2K). Collectively, we deciphered the cellular composition, interaction, and transition of the tumor immune environment in MSS CRC at single-cell resolution, which helped us to deeply understand the immune characteristics and identify different subtypes of MSS tumor.

3.4 Spatial and peripheral blood single-cell transcriptomic landscape in MSS CRC

Given the complexity of TME structure, we subsequentially analyzed CRC ST data to explore the spatial distribution of different immune cells. We first used the unsupervised clustering method to classify the spatial spots into different clusters, and then we identified distinct regions, including normal epithelial, hepatocytes, tumor, stromal, and immune cell regions, according to H&E staining sections and the integration of previous scRNA-seq annotation data (Figure 3A, S1A and S4A). Notably, due to a spatial spot containing about 10 cells, we observed several cell types colocalized at same spots in some regions, such as malignant/immune cells, immune/stromal cells, and malignant/stromal cells, indicating a physical interaction between these cell types. Further, we quantified the spatial distribution of MSS tumor-enriched immune cell subtypes based on their DEGs and well-known marker genes from previous scRNA-seq results (Figure 3A, S4A, Table S5 and S7). In primary tumors, we found T, NK, and plasma cells distributed locally in the stromal region, surrounded by abundant fibroblasts or lamina propria, suggesting that these effective immune cells found it difficult to infiltrate into the tumor parenchyma (Figure 3A). By contrast, monocytes were more widely enriched in tumor regions, consisting of the cell-chat results of an extensive interaction between monocytes and tumor cells (Figure 2J). These results demonstrated a significant spatial intra-tumoral immune infiltration heterogeneity in MSS CRC.

Most TME-infiltrated immune cells derived from peripheral blood; therefore, we also analyzed the scRNA-seq data containing blood samples of CRC patients. After unsupervised clustering, we obtained a total of 16 immune cell subtypes, and the majority of these cell types were consistent with our previous annotated cell types from MSS CRC (Figure 2A, 2G, 3B-C). The NK, monocytes, naïve CD4T, and effector memory CD4T cells showed a strong distribution preference in peripheral blood, while functional and terminally differentiated T cells and macrophages appeared to be tissue-enriched, and the pseudotime trajectory also presented an immune cell differentiation trend from peripheral blood to the tissue (Figure 3D-E and Table S9). Interestingly, we found a significantly positive correlation between the abundance of several immune cell subtypes from blood and tumor tissue, including naïve CD4T, CD4Treg, cytotoxic CD8T, CD4Th17, and B cells (Figure 3F and S4B). Therefore, we concluded that the content of these cell subsets in peripheral blood could reflect the cell infiltration level in the TME, which provided the feasibility of liquid biopsy-based biomarker screening. Altogether,

we comprehensively analyzed and discovered the immune characteristics of MSS CRC tumors from three dimensions including tissue spatial distribution and tissue and peripheral blood single-cell transcriptomics.

3.5 Identification of MSS CRC immune cell-related modules and hub genes

To further identify the MSS CRC immune cell-related modules and hub genes, the WGCNA procedure was used to explore the gene modules related to three main MSS CRC-enriched immune cell types including T cells (composed of naïve CD4T, CD4Treg, CD4Th17, exhausted CD8T, cytotoxic CD8T, proliferated CD8T, and NK cells), plasma cells, and monocytes (composed of classical and intermediated monocytes). First, to obtain the signature of the three main immune cell types, we selected the top DEGs of each cell subtype from the scRNA-seq data as markers and then calculated the immune cell infiltration level for each patient using the GSVA algorithm on the TCGA-CRC cohort (Table S5 and S7). Obviously, three signatures could properly represent the three main immune cell types, and the survival analysis showed that higher T and plasma cells and lower monocytes infiltration were associated with superior OS (Figure 4A-F). We then set the soft threshold β as 9 ($R2 = 0.908$) to provide a suitable power value for co-expression network construction (Figure S5A). Eighteen modules indicated by different colors were determined by dynamic tree (Figure S5B). In addition, the correlations between modules and three immune cell type infiltration were calculated. Interestingly, we observed that the darkgreen module had the highest correlation with the infiltration of all three immune cell types in the module–trait relationship (Figure 4G). In this module, the correlation coefficients between GS and MM reached 0.69, 0.67, and 0.82, respectively, suggesting a good quality of module construction (Figure 4H-J). To identify the hub genes derived from three immune cell types infiltration within the darkgreen module, 816 genes with $GS > 0.5$ and $MM > 0.6$ were considered hub genes. With the intersection of DEGs of MSS CRC-enriched immune cell subtypes from scRNA-seq data, a total of 108 overlapping genes were extracted for subsequent analyses (Figure 4K).

3.6 Construction of MSS CRC immune cell-related signature

Based on the expression profiles of 108 MSS CRC immune cell-related genes, we performed a multivariate Cox regression analysis to identify prognostic genes, adjusting by age, gender, and TNM stage. In order to ensure the stability of OS-related genes, we used the random-effects model of systematic meta-analysis to pool the HR values of 108 hub genes in three independent MSS CRC cohorts (TCGA-CRC [n=418], GSE39582 [n=459], and GSE41258 [n=137]). Finally, we obtained 39 stable significantly prognostic immune cell-related genes for MSS CRC patients (meta-$P < 0.001$, Figure 5A). Thirty-nine genes were then subjected to the machine learning-based integrative procedure to develop an MSS CRC immune cell-related signature (MCICRS). Based on 10 machine learning algorithms, we fitted a total of 96 kinds of prediction models with 10-fold cross-validation, and calculated the C-index of each model across the TCGA-CRC training dataset, and three independent validation datasets (GSE39582 [n=459], GSE39084 [n=54], and GSE41258 [n=137]). Here, we found the combination of RSF and stepwise Cox (direction = forward) algorithms had the best performance with the highest average C-index (0.681) in all datasets (Figure 5B and Table S10). A final set of 13 top genes were filtrated in the RSF model and were then subjected to the stepwise Cox proportional hazards regression model to obtain their corresponding regression coefficients (Figure 5C-E). Next, based on the expression of 13 genes weighted by their regression coefficients, we calculated the MCICRS for each MSS CRC patient, and assigned them into high- and low-MCICRS groups according to the optimal cut-off value. In the TCGA-CRC cohort, patients with low-MCICRS had a significantly prolonged OS ($P < 0.05$), and the multivariate Cox regression analysis indicated that MCICRS was an independent and significant risk factor for OS after adjusting for age, gender, metastasis, and TNM stage (Figure 5F-G). In addition, we evaluated the predictive value of MCICRS in OS and RFS in all six GEO datasets and the GEO-meta cohort, and found the same trend (Figure 5H-I and S6). Moreover, we compared the performance of MCICRS with other existing signatures from published literature and prior research and, ultimately, 104 signatures associated with various biological processes were enrolled, including immune response, autophagy, and epithelial–mesenchymal transition (Table S11). Based on univariate Cox regression, we compared the C-index of MCICRS with other signatures across four datasets. Notably, MCICRS displayed a better performance than most other signatures in the three datasets except GSE39084, which demonstrated the stability of MCICRS (Figure S7).

3.7 Immune infiltration characteristics of MCICRS and its implication in immunotherapy

Since the construction of MCICRS was based on the immune cell-related genes, we assumed that there existed distinct immune characteristics between high- and low-MCICRS groups, which may explain their prognostic differences. According to the ssGSEA method, we found a higher infiltration abundance of 28 immune cells in the low-MCICRS group (Figure 6A). To ensure that the assessments were not biased by the single algorithm, five other methods—including EPIC, MCP-counter, quanTIseq, TIMER, and xCell—were used to verify the stability and robustness of the ssGSEA results (Figure S8). In addition, the ESTIMATE method also showed a higher immune score in the low-MCICRS group (Figure 6B). Further, GSEA and GSVA analyses demonstrated that several immune-related pathways were activated in the low-MCICRS group, such as cytokine, chemokine, TNFA, and interferon signaling pathways (Figure 6C-D). In addition, scatter plots of MCICRS and CD274 demonstrated a positive correlation in the scRNA-seq data (Figure S9A). We also calculated the MCICRS score of each spot in the ST data, and found a consistent spatial distribution with the immune cells (Figure S9B). We also used Proteomap, a graphical tool to quantitate and visualize the composition and function of proteomes, to compare the differences between high- and low-MCICRS groups. Interestingly, the pattern of the proteomap in the low-MCICRS group showed a higher enrichment of proteins related to Jak/STAT, cytokine–cytokine receptor interaction, and NF-κB and TNF signaling pathways compared to the high-MCICRS group (Figure 6E). Collectively, these results confirmed an activated immune status in low-MCICRS patients, hence, we inferred that MCICRS could predict the immunotherapy effects in MSS CRC. The GSE179351 study evaluated the efficacy of combining radiation, ipilimumab, and nivolumab in MSS CRC patients (Parikh et al., 2021). After applying the MCICRS to the RNA-seq data from pre-treatment biopsies samples, we observed a prolonged OS in low-MCICRS patients, although the statistical difference was not significant due to the small sample size (Figure 6F). Furthermore, we enrolled 22 public immunotherapy cohorts with treatment response or survival data to assess the predictive value of MCICRS in immunotherapy across pan-cancer types using a systematic meta-analysis. Strikingly, we observed that a higher MCICRS was significantly associated with the progression of treatment response and dismal survival when the OR and HR values of each cohort were pooled in the random-effects model, indicating that MCICRS was a reliable biomarker for immunotherapy (Figure 6G-H).

3.8 Validation of MCICRS in clinical outcomes of in-house immunotherapy cohort

To further validate the prognostic value of MCICRS in MSS CRC patients receiving immunotherapy, we first calculated the level of MCICRS in 38,508 cells from 19 MSS CRC tumor samples at single-cell resolution. Surprisingly, the MCICRS value was higher in myeloid cells while being lower in T and B cells, indicating that high lymphocytes and low myeloid cells in patients may be associated with superior survival (Figure 7A-B). In addition, the majority of TME-enriched immune cells were derived and differentiated from peripheral blood immune cells, and the abundance of these cell types between blood and tumor tissue had a positive correlation (Figure 3F). Therefore, we considered that peripheral blood lymphocytes and monocytes could reflect the TME immune cells infiltration and serve as biomarker candidates for MSS CRC patients receiving immunotherapy. Here, we detect the peripheral blood lymphocytes and monocytes counts of 54 MSS CRC patients at the initiation of immunotherapy treatment via hematology analyzer. Likewise, we found patients with higher lymphocytes and lower monocytes exhibited a better treatment response (PR and SD) and preferable PFS (Figure 7C-G). After adjusting for the confounding factors, including age, gender, ECOG performance status, primary tumor location, lung metastasis, and liver metastasis, the lymphocytes and monocytes counts remained statistically significant for PFS, supporting the supposition that these two immune cell types were independent predictors for immunotherapy in MSS CRC (Figure 7H). Finally, we developed a nomogram based on lymphocytes, monocytes, and three significant clinical characteristics in a multivariable Cox model with an excellent predictive accuracy: the AUCs for predicting PFS at 6, 12, and 18 months were 0.798, 0.797, and 0.845, respectively (Figure 7I-J).

4 Discussion

In this study, we confirmed an improved efficacy and survival benefit of anti-PD-1 antibody combined

with VEGFRi in MSS CRC patients, with a manageable toxicity. Based on CRC scRNA-seq and spatial transcriptomic data, we comprehensively deciphered the cell composition, interactions, differentiations, and spatial distribution characteristics, and further identified MSS CRC-enriched immune cell subtypes. Through a machine learning-based integration, MCICRS was developed to accurately predict the efficacy and clinical outcomes for MSS CRC patients receiving immunotherapy.

VEGF-driven angiogenesis affected immune suppression at many different levels, including inhibiting the antigen-presenting cells (APC) and effector T cells while augmenting the expansion of immune suppressive cells such as Tregs and MDSC (Rahma and Hodi, 2019). Emerging evidence indicates that the combination of immunotherapy and anti-angiogenic agents could reverse the immune suppression driven by VEGF-related pathways in melanoma, renal cell carcinoma, non-small cell lung cancer, and hepatocellular carcinoma (Hodi et al., 2014; Mcdermott et al., 2018; Socinski et al., 2018; Finn et al., 2020). However, the application of this combination strategy was limited in clinical practice for MSS CRC patients. Recently, three clinical trials, including REGONIVO, REGOMUNE, and Kim et al.'s study, presented encouraging anti-tumor activity of regorafenib combined with nivolumab or avelumab (anti-PD-L1 antibody) in MSS CRC, with the DCR ranging from 54% to 86% (Fukuoka, et al., 2020; Cousin, et al., 2021; Kim, et al., 2022). Mechanically, our scRNA-seq and spatial transcriptomic data demonstrated a complex interaction between VEGF-driven angiogenic signaling and immune checkpoint-related immunosuppression, shown by the co-localization of VEGFB+ myeloid cells and exhausted CD8+T cells, which provided a theoretical basis for the potential effect of an immunotherapy and anti-angiogenic therapy combination. As expected, our retrospective study also manifested an improved clinical benefit of anti-PD-1 antibody plus VEGFRi treatment. For MSS CRC treated with combination therapy, we observed 63% of DCR, 4.4 months of median PFS, and 10.2 months of median OS, which were highly consistent with the results of REGOMUNE (53% of DCR, 3.6 months of median PFS, and 10.8 months of median OS) and Kim et al.'s study (63% of DCR, 4.3 months of median PFS, and 11.1 months of median OS) (Cousin, et al., 2021; Kim, et al., 2022). These outcomes were all inferior to those of the REGONIVO study; the main reasons we considered were as follows: firstly, more than 70% of the patients in our study had liver metastasis compared to 50% of those in the REGONIVO study, which was an independent risk factor for CRC patients (Engstrand et al., 2018). Secondly, RAS mutation could impair the treatment effectiveness and prognosis of CRC and, in our study, the number of patients carrying the RAS mutation was almost twice that of those in the REGONIVO study (46.3% vs. 24%) (Karapetis et al., 2008). Thirdly, the ECOG performance status of all patients in REGONIVO were 0, whereas half of the patients in this study were 2. In this current study, more than half of the patients with SD had a certain degree of tumor shrinkage, and these patients might achieve PR after receiving further cycles of treatment. In addition, in the survival analysis, anti-PD-1 antibody plus VEGFRi combination brought about a 50% decrease in both disease progression risk and death risk compared to VEGFRi alone. In addition, the treatment-related AEs profile in this study was consistent with previous clinical trials (Fukuoka, et al., 2020; Cousin, et al., 2021; Kim, et al., 2022), and the incidence rate between the combination and VEGFRi groups was similar across the majority of AEs. Based on the above results, we considered that anti-PD-1 antibody combined with VEGFRi presented a better efficacy and controllable toxicity in MSS CRC compared to VEGFRi alone.

In most scenarios, only 20–40% of patients responded to immunotherapy and even fewer had long-term disease remission. Therefore, a biomarker-based guide to identify subsets who could benefit from immunotherapy is vitally critical. Currently, PD-L1 expression is the most widely accepted biomarker for guiding the selection of patients to receive anti-PD-1 or anti-PD-L1 antibodies (Doroshow et al., 2021). However, REGONIVO did not observe a clear relationship between PD-L1 expression and efficacy outcomes in MSS CRC and, therefore, additional analyses were necessary to clarify the optimal patient population for immunotherapy (Fukuoka, et al., 2020). In consideration of the fact that TME-infiltrated immune cells were the main effectors of immunotherapy, we in this study identified 10 MSS CRC-enriched immune cell subtypes and their spatial distribution, including naïve CD4T, CD4Treg, CD4Th17, exhausted CD8T, cytotoxic CD8T, proliferated CD8T, NK, and IgG plasma cells, and classical and intermediate monocytes, through scRNA-seq along with spatial transcriptomic data. In addition, through WGCNA and marker genes of these MSS CRC-enriched immune cell subtypes, we identified MSS CRC immune cell-related hub genes. Based on the expression profile of hub genes, we first determined 39 stable prognostic genes via meta-analysis in three independent cohorts. Then, a total of 96 kinds of prediction model were fitted in the TCGA-CRC training set and three validation sets. After calculating the C-index across all four datasets, we obtained the optimal model of a combination of RSF and

stepwise Cox (direction = forward) algorithms, and further developed the MCICRS. Based on a variety of machine learning methods, the integrative procedures used in this study presented the advantage of a fitting prognostic model for MSS CRC, and method combinations could further reduce the dimensionality of variables, making the model more simplified and translational. The following analyses proved that a higher MCICRS was a deleterious indicator of OS and RFS in MSS CRC patients, with inferior immune infiltration and immune-related pathway activity. The meta-analysis of pan-cancer immunotherapy also demonstrated that MCICRS maintained high accuracy and a stable performance in predicting immunotherapy efficacy and survival, indicating a great potential for the clinical application of MCICRS.

Several hub genes of MCICRS had been reported to relate to the efficacy of immunotherapy. For example, S100A12 is a S100/calgranulin protein, and its high expression has been proven to correlate with the survival of HPV-negative hypopharyngeal squamous cell carcinoma in immunotherapy (Mints et al., 2021). MS4A4A was a member of the membrane-spanning 4A family, and was selectively highly expressed in tumor-associated macrophages, which could regulate the immune escape of tumor cells via promoted M2 polarization of macrophages by activating the PI3K/AKT pathway and the JAK/STAT6 pathway (Li et al., 2023). A previous study demonstrated that GZMK+ effector memory T cells and CXCL13+BHLHE40+ TH1-like cells were preferentially enriched in MSI-H CRC, which explained their favorable responses to immunotherapy (Zhang et al., 2018). APOBEC3A is a member of the apolipoprotein B messenger RNA-editing, enzyme-catalytic, polypeptide-like 3 family and plays an important role in the innate immune response, and a higher enrichment score of APOBEC3A mutagenesis correlated with favorable prognosis, immune activation, and potential immunotherapy response in bladder cancer (Shi et al., 2022). The glycoprotein CD2 was a costimulatory receptor expressed mainly on T and NK cells, and had an important role in the formation and organization of the immunological synapse. The interaction of CD58 and CD2 was required for anti-tumor immunity and was predictive of immunotherapy response; defects in this axis promoted immune evasion through diminished T cell activation and impaired intra tumoral T cell infiltration and proliferation, and concurrently increased PD-L1 protein stabilization (Ho et al., 2023). A previous study also revealed that CXCL9 was significantly upregulated following dual PD-1/CTLA-4 blockade (House et al., 2020). Our research demonstrated that those immune-related genes were associated with the survival of CRC, and are a potential biomarker of immunotherapy.

Peripheral blood-derived biomarkers have the advantages of being non-invasive and easily accessible compared to tissue biopsy (Zhou et al., 2022). To further validate and expand the implementation of MCICRS, we identified a higher MCICRS in monocytes while a lower MCICRS in lymphocytes at single-cell resolution. Additionally, in a house cohort of MSS CRC treated with immunotherapy, we verified that patients with higher lymphocytes and lower monocytes exhibited a better treatment response and preferable PFS, suggesting the content of both immune cell types could reflect MCICRS level and be favorable surrogates for routine immunotherapy biomarkers like PD-L1 expression. The above results transferred the MCICRS model into peripheral blood lymphocytes and monocytes abundance, making it easily available in clinical practice to expand its usage, and validated it as a potential candidate biomarker for selecting suitable MSS CRC patients who could benefit from immunotherapy.

There are several limitations of this study that need to be acknowledged. First, it was a retrospective study with a small sample size. A prospective study with large populations is necessary to further evaluate the efficacy and safety of the anti-PD-1 antibody and VEGFRi combination in MSS CRC. Second, due to the restriction of the tissue samples, we could not assess the MCICRS for each MSS CRC patient. Our future prospective study would collect the tissue samples and validate the predictive value of MCICRS. Finally, the detailed functions of the constituent genes of MCICRS in CRC need to be revealed in further with in vivo and in vitro experiments.

5 Conclusions

In conclusion, anti-PD-1 antibody combined with VEGFRi presented improved efficacy and survival in MSS CRC with manageable toxicity. Based on analyses of scRNA-seq and spatial transcriptomic data and machine learning algorithms, we developed a stable and powerful signature for accurately assessing the efficacy and prognosis of MSS CRC patients receiving immunotherapy, which could be a promising tool for optimizing decision-making for individual patients.

Acknowledgements

We thank to KS official accounts team (Zhejiang University, Hangzhou, China) for their help of data analysis and visual codes. We also thank Dr. Siyuan Huang (Academy for Advanced Interdisciplinary Studies, Peking University, Beijing, China) for his help of data analysis and visual codes.

Author Contributions

Conception and design: JZ, XW and HL; Development of methodology: SY, YX and GD; Acquisition of data: SY, YX and GD, SR, RH, YG, QQ, CW, SQ and YX; Analysis: SY, YX, GD, SR and RH; Interpretation of results: SY, YX and GD; Writing, revision and review of the manuscript: SY, YX, GD, SR, RH, XX, JZ, XW and HL; Study supervision: JZ, XW and HL. All authors read and approved the final manuscript.

Compliance with ethics guidelines

The authors declare that they have no conflict of interest for this work. And this study was approved by the Ethics Committee of Sir Run Run Shaw Hospital (The certificate no. 20190211-55).

Availability of data and materials

The in-house dataset used and analyzed in this study are available from the corresponding author on reasonable request. Other public data analyzed in this study are available from The Cancer Genome Atlas (TCGA, https://portal.gdc.cancer.gov/), and Gene Expression Omnibus (GEO, https://www.ncbi.nlm.nih.gov/geo/).

Funding

Project supported by the National Natural Science Foundation of China (Grant No. 81972012).

Figure 1. Immunotherapy combined with anti-angiogenic therapy improved the clinical outcomes of MSS CRC patients.

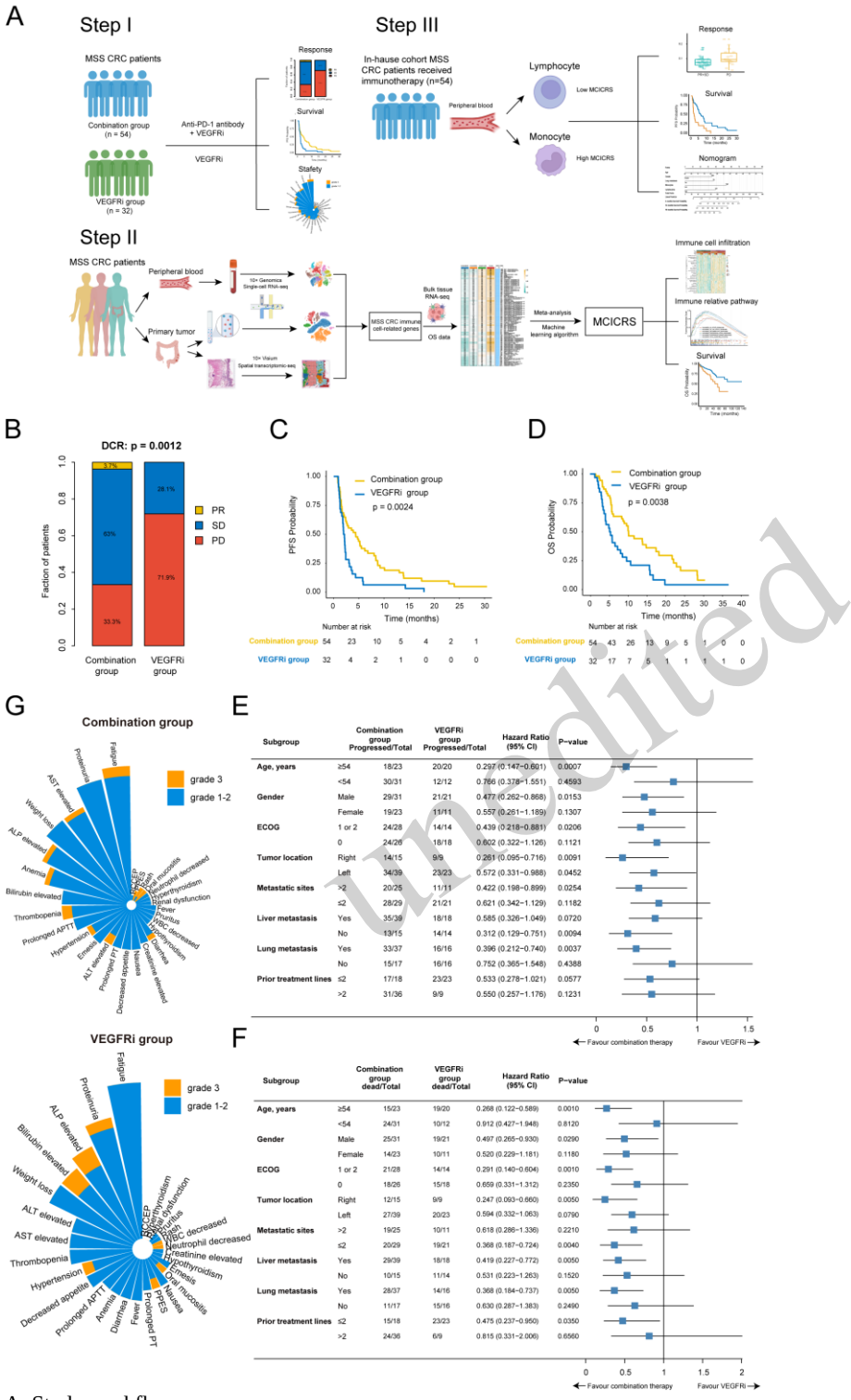

A. Study workflow.

B. The treatment response comparison of the combination group and the VEGFRi group (DCR: 66.7% vs 28.1%, P=0.012, Chi square test).

C-D. Kaplan–Meier analysis of PFS C) and OS D) in the combination group and the VEGFRi group (log-rank test).

E-F. Subgroup analysis of PFS E) and OS F) in the combination group and the VEGFRi group.

G. Adverse events of any grade in the combination group and the VEGFRi group.

Figure 2. A single-cell transcriptomic atlas in MSS CRC tumor immune microenvironment.

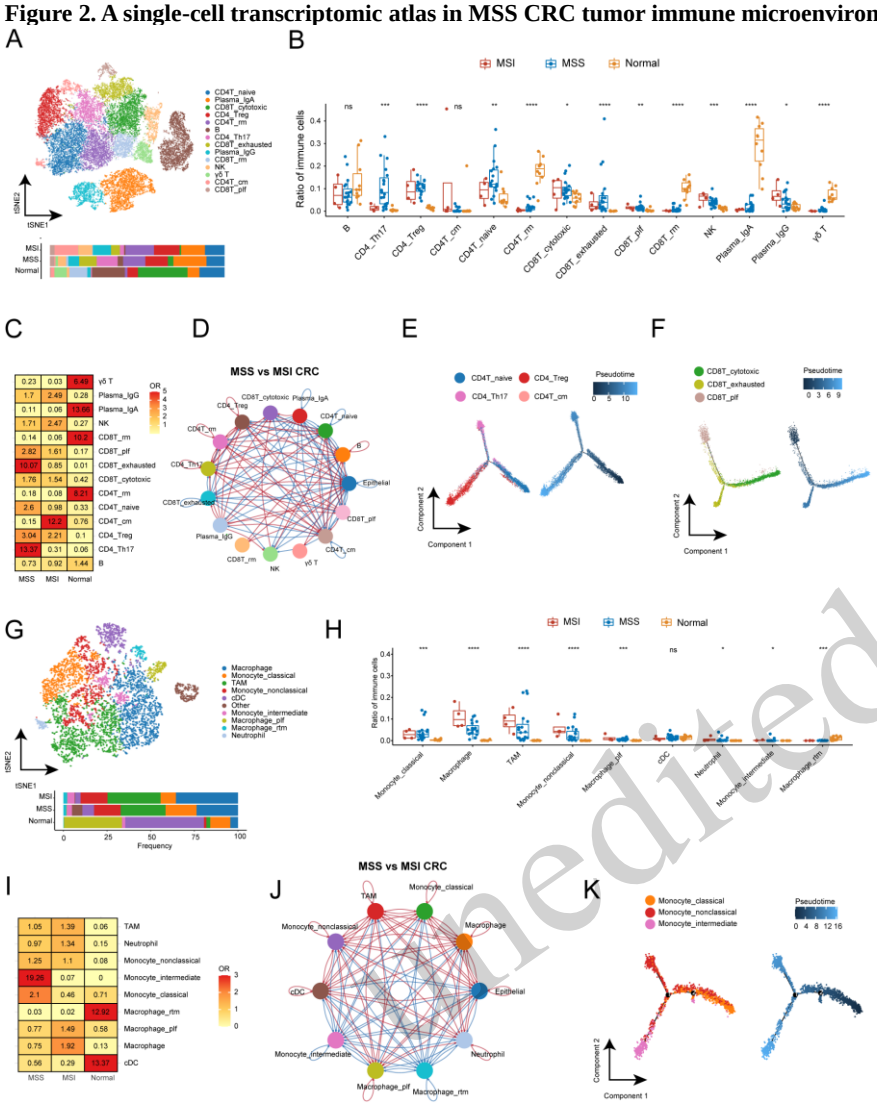

A. t-SNE plot of lymphoid-derived cell subtypes of CRC patients. Each cluster is color-coded according to cell type. Cluster annotations and comparison of proportion are indicated in the figure.

B. Boxplot of lymphoid-derived cell subtypes fraction in MSI tumor (red), MSS tumor (blue), and normal tissue (green) (Kruskal–Wallis test).

C. Heatmap showing the OR value of each lymphoid-derived cell subtype in MSI tumor, MSS tumor, and normal tissue.

D. Comparison of cell–cell communications of malignant epithelial and lymphoid-derived cell subtypes between MSS and MS1 tumor by cell-chat analysis. Blue indicates a higher interaction weight in MSS tumor, and red indicates a higher interaction weight in MSI tumor.

E. Pseudotime analysis of CD4+T cells from MSS CRC patients. CD4+T cell subtypes are labeled by colors.

F. Pseudotime analysis of CD8+T cells from MSS CRC patients. CD8+T cell subtypes are labeled by colors.

G. t-SNE plot of myeloid-derived cell subtypes of CRC patients. Each cluster is color-coded according to cell type. Cluster annotations and a comparison of the proportion are indicated in the figure.

H. Boxplot of myeloid-derived cell subtypes fraction in MSI tumor (red), MSS tumor (blue), and normal tissue (green) (Kruskal–Wallis test).

I. Heatmap showing the OR value of each myeloid-derived cell subtype in MSI tumor, MSS tumor, and normal tissue.

J. Comparison of cell–cell communications of malignant epithelial and myeloid-derived cell subtypes between MSS and MS1 tumors by cell-chat analysis. Blue indicates a higher interaction weight in MSS tumor, and red indicates a higher interaction weight in MSI tumor.

K. Pseudotime analysis of monocyte from MSS CRC patients. Monocyte subtypes are labeled by color.

Figure 3. Spatial and peripheral blood single-cell transcriptomic landscape in MSS CRC.

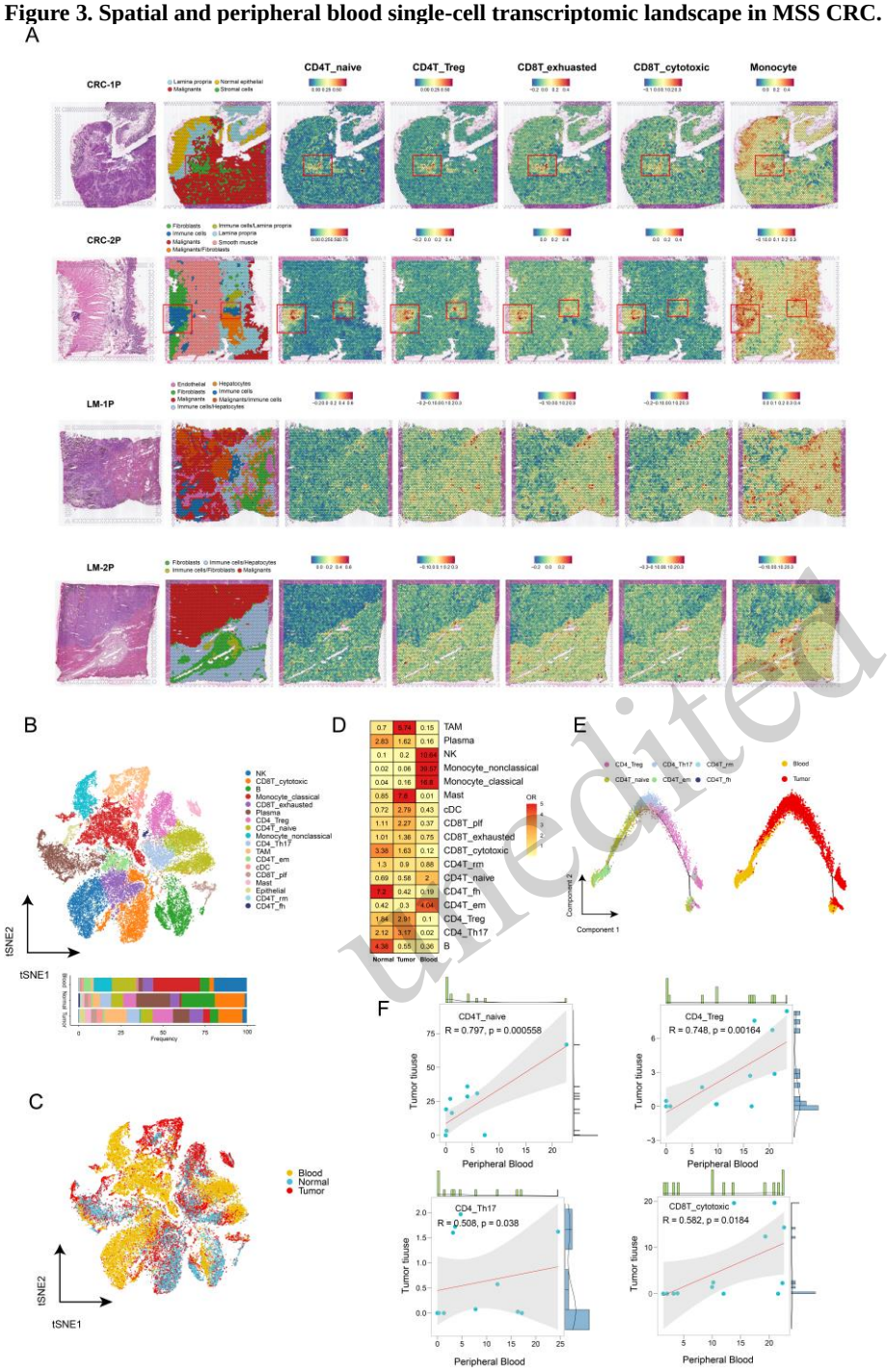

A. The H&E staining section, unsupervised clustering analysis, and MSS CRC-enriched immune cell distribution of spatial transcriptomic data from CRC patients with primary tumor and liver metastasis.

B. t-SNE plot of immune cell subtypes of CRC patients. Each cluster is color-coded according to cell type. Cluster annotations and a comparison of the proportion are indicated in the figure.

C. t-SNE plot of immune cell subtypes from tumor, normal and peripheral blood samples of CRC patients. Each cluster is color-coded according to cell type. Cluster annotations and a comparison of the proportion are indicated in the figure.

D. Heatmap showing the OR value of each immune cell subtype in tumor, normal, and peripheral blood samples of CRC patients.

E. Pseudotime analysis of CD4+T cells from MSS CRC patients. CD4+T cell subtypes are labeled by color.

F. The Pearson correlation of MSS CRC-enriched immune cell type proportion from tumor and peripheral blood samples.

Figure 4. Identification of MSS CRC immune cell-related modules and hub genes.

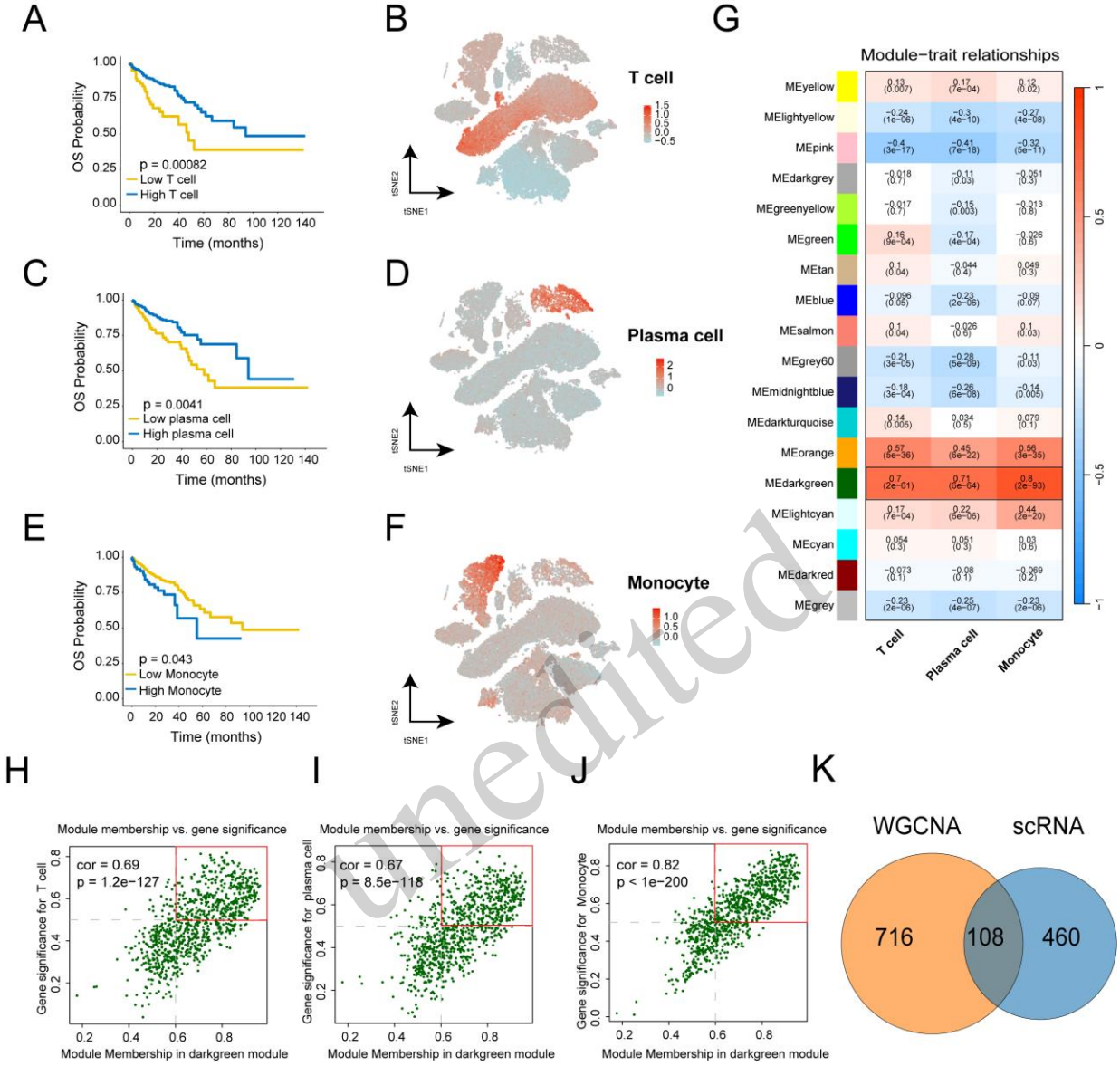

A. The OS analysis for the MSS TCGA-CRC cohort with different T cell infiltrations (log-rank test).
B. The expression level of T cell signature in t-SNE plot.
C. The OS analysis for the MSS TCGA-CRC cohort with different plasma cell infiltrations (log-rank test).
D. The expression level of plasma cell signature in t-SNE plot.
E. The OS analysis for the MSS TCGA-CRC cohort with different monocyte infiltrations (log-rank test).
F. The expression level of monocyte signature in t-SNE plot.
G. Correlation analysis between module eigengenes and immune infiltration of T cell, plasma cell, and monocyte.
H-J. The high correlation between GS of T cell H), plasma cell I), and monocyte J) and MM in the darkgreen module. Dots within the red rectangle were defined as immune cell-related genes, with both high GS and MM.
K. The overleaping immune cell-related genes between WGCNA and scRNA-seq data.

Figure 5. Construction of MSS CRC immune cell-related signature.

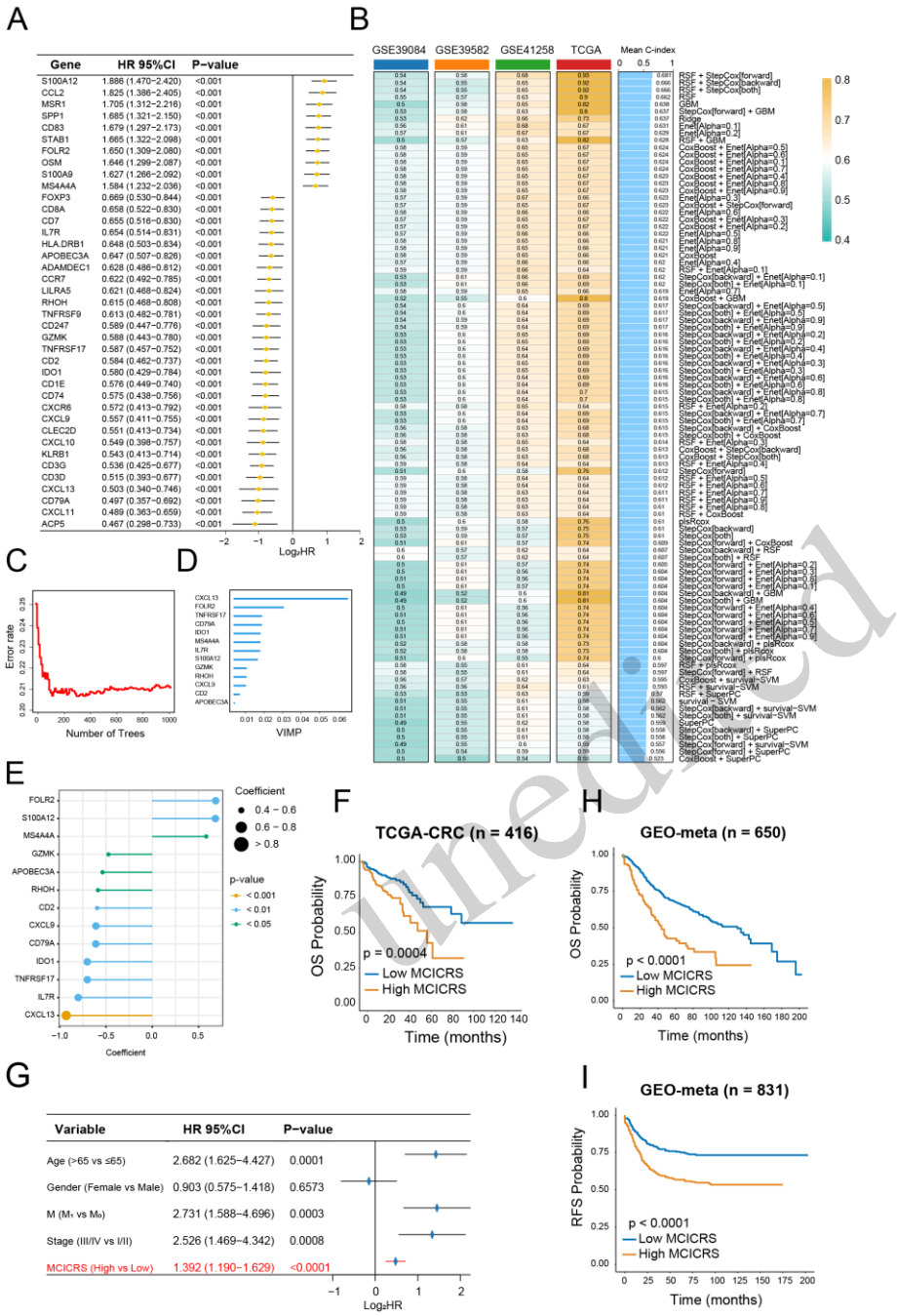

A. The forest plot showing the pooled HR from meta-analysis of prognostic immune cell-related genes.

B. A total of 96 kinds of prediction models based on machine learning methods and further calculations of the C-index of each model across training and validation datasets.

C-D. The number of trees for determining the minimal error C) and the importance D) of the 13 most valuable genes based on the RSF algorithm.

E. Coefficients of 13 genes finally obtained in the stepwise Cox regression model.

F. The OS analysis according to MCICRS for the TCGA-CRC cohort (log-rank test).

G. Multivariable Cox regression analysis indicates that MCICRS is an independent risk factor for OS in the TCGA-CRC cohort.

H. The OS analysis according to MCICRS for the GEO-meta cohort (log-rank test).

I. The RFS analysis according to MCICRS for the GEO-meta cohort (log-rank test).

Figure 6. Immune infiltration characteristics of MCICRS and its implication in immunotherapy.

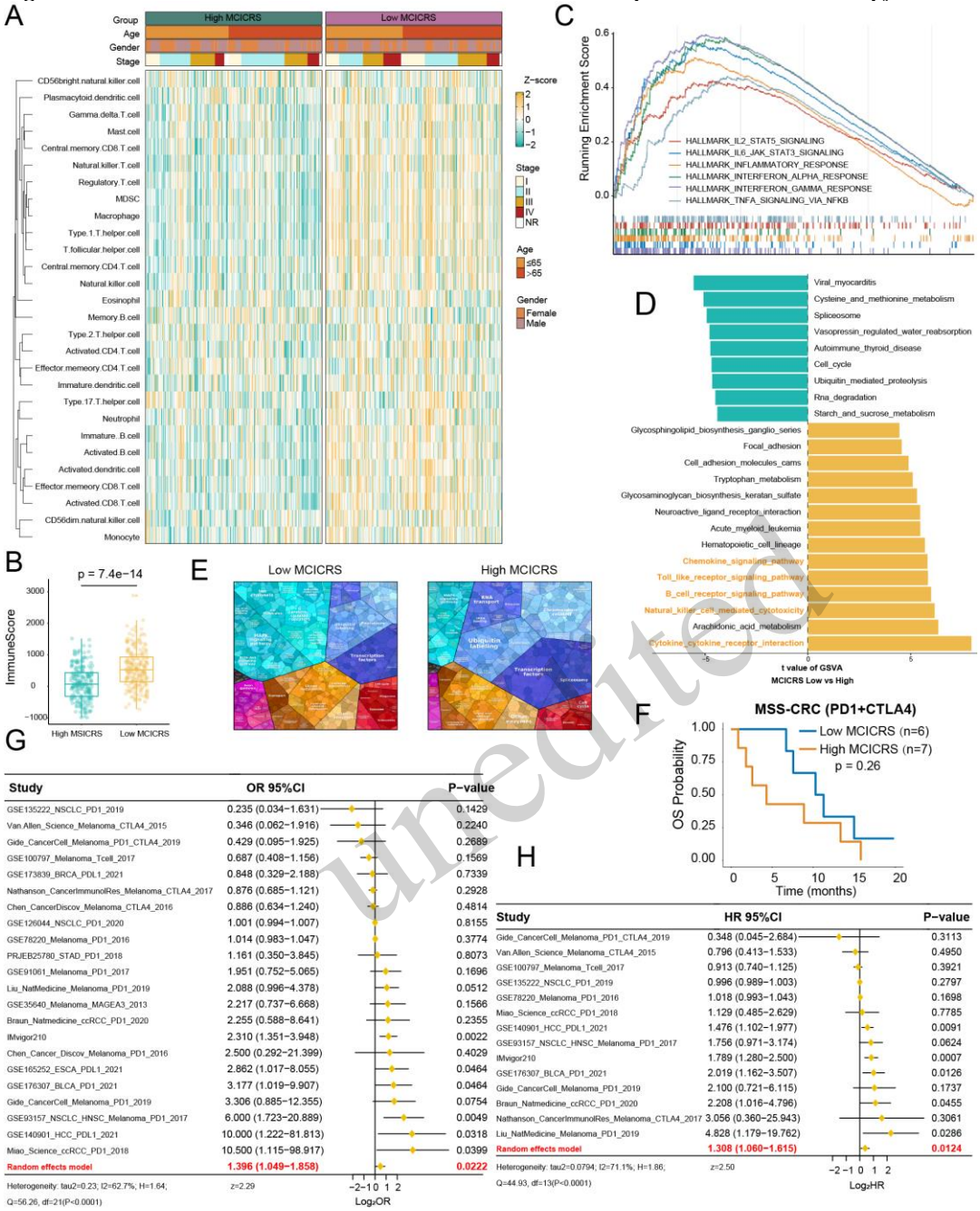

A. The infiltration abundance of 28 immune cell subsets evaluated by ssGSEA for MCICRS-low and -high groups.

B. The distribution of immune score inferred by the ESTIMATE algorithm between MCICRS-low and -high groups (Wilcoxon test).

C-D. GSEA enrichment analysis C) and GSVA analysis D) showing the activation status of immune-related pathways in MCICRS-low group.

E. Online proteomaps analysis showing the KEGG pathway activation between MCICRS-low and -high groups.

F. The OS analysis according to MCICRS for MSS CRC patients receiving immunotherapy (log-rank test).

G. The meta-analysis showing high MCICRS is significantly associated with progression of immunotherapy response across pan-cancer types.

H. The meta-analysis showing high MCICRS is significantly associated with inferior survival of immunotherapy response across pan-cancer types.

Figure 7. Validation of MCICRS in clinical outcomes of in-house immunotherapy cohort.

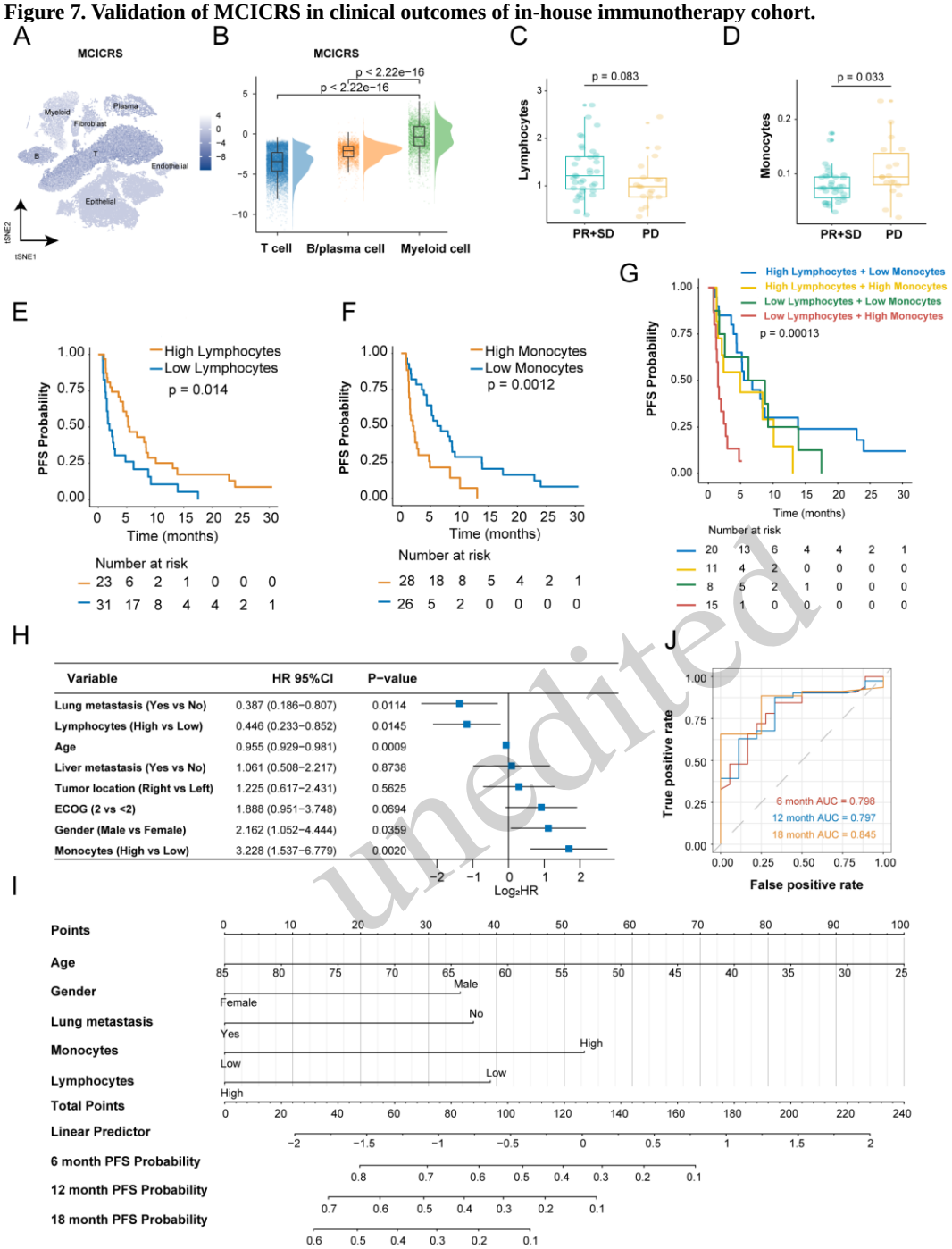

A. The MCICRS level across main cell types of CRC in t-SNE plot.

B. The comparison of MCICRS between myeloid cells and T and B/plasma cells (Wilcoxon test).

C-D. The comparison of peripheral blood lymphocytes C) and monocytes D) between PR+SD group and PD group for MSS CRC patients receiving immunotherapy (t test).

E-G. The PFS analysis according to lymphocytes C), monocytes D), and both G) level for MSS CRC patients receiving immunotherapy (log-rank test).

H. Multivariable Cox regression analysis indicates that high lymphocytes and low monocytes are an independent factor for superior OS in MSS CRC patients receiving immunotherapy.

I. Nomogram for predicting progression probability for MSS CRC patients receiving immunotherapy.

J. Time-dependent ROC analysis for predicting PFS at 6, 12, and 18 months for MSS CRC patients receiving immunotherapy.

References

Andre T, Shiu KK, Kim TW, et al., 2020. Pembrolizumab in microsatellite-instability-high advanced colorectal cancer. N Engl J Med, 383(23):2207-2218. https://doi.org/10.1056/NEJMoa2017699

Butler A, Hoffman P, Smibert P, et al., 2018. Integrating single-cell transcriptomic data across different conditions, technologies, and species. Nat Biotechnol, 36(5):411-420. https://doi.org/10.1038/nbt.4096

Colaprico A, Silva TC, Olsen C, et al., 2016. Tcgabiolinks: An r/bioconductor package for integrative analysis of tcga data. Nucleic Acids Res, 44(8):e71. https://doi.org/10.1093/nar/gkv1507

Cousin S, Cantarel C, Guegan JP, et al., 2021. Regorafenib-avelumab combination in patients with microsatellite stable colorectal cancer (regomune): A single-arm, open-label, phase ii trial. Clin Cancer Res, 27(8):2139-2147. https://doi.org/10.1158/1078-0432.CCR-20-3416

Doroshow DB, Bhalla S, Beasley MB, et al., 2021. Pd-l1 as a biomarker of response to immune-checkpoint inhibitors. Nat Rev Clin Oncol, 18(6):345-362. https://doi.org/10.1038/s41571-021-00473-5

Engstrand J, Nilsson H, Stromberg C, et al., 2018. Colorectal cancer liver metastases - a population-based study on incidence, management and survival. BMC Cancer, 18(1):78. https://doi.org/10.1186/s12885-017-3925-x

Finn RS, Qin S, Ikeda M, et al., 2020. Atezolizumab plus bevacizumab in unresectable hepatocellular carcinoma. N Engl J Med, 382(20):1894-1905. https://doi.org/10.1056/NEJMoa1915745

Fukuoka S, Hara H, Takahashi N, et al., 2020. Regorafenib plus nivolumab in patients with advanced gastric or colorectal cancer: An open-label, dose-escalation, and dose-expansion phase ib trial (regonivo, epoc1603). J Clin Oncol, 38(18):2053-2061. https://doi.org/10.1200/JCO.19.03296

Grothey A, Van Cutsem E, Sobrero A, et al., 2013. Regorafenib monotherapy for previously treated metastatic colorectal cancer (correct): An international, multicentre, randomised, placebo-controlled, phase 3 trial. Lancet, 381(9863):303-312. https://doi.org/10.1016/S0140-6736(12)61900-X

Ho P, Melms JC, Rogava M, et al., 2023. The cd58-cd2 axis is co-regulated with pd-l1 via cmtm6 and shapes anti-tumor immunity. Cancer Cell, 41(7):1207-1221 e1212. https://doi.org/10.1016/j.ccell.2023.05.014

Hodi FS, Lawrence D, Lezcano C, et al., 2014. Bevacizumab plus ipilimumab in patients with metastatic melanoma. Cancer Immunol Res, 2(7):632-642. https://doi.org/10.1158/2326-6066.CIR-14-0053

House IG, Savas P, Lai J, et al., 2020. Macrophage-derived cxcl9 and cxcl10 are required for antitumor immune responses following immune checkpoint blockade. Clin Cancer Res, 26(2):487-504. https://doi.org/10.1158/1078-0432.CCR-19-1868

Jin S, Guerrero-Juarez CF, Zhang L, et al., 2021. Inference and analysis of cell-cell communication using cellchat. Nat Commun, 12(1):1088. https://doi.org/10.1038/s41467-021-21246-9

Karapetis CS, Khambata-Ford S, Jonker DJ, et al., 2008. K-ras mutations and benefit from cetuximab in advanced colorectal cancer. N Engl J Med, 359(17):1757-1765. https://doi.org/10.1056/NEJMoa0804385

Kim RD, Kovari BP, Martinez M, et al., 2022. A phase i/ib study of regorafenib and nivolumab in mismatch repair proficient advanced refractory colorectal cancer. Eur J Cancer, 169:93-102. https://doi.org/10.1016/j.ejca.2022.03.026

Langfelder P, Horvath S, 2008. Wgcna: An r package for weighted correlation network analysis. BMC Bioinformatics, 9:559. https://doi.org/10.1186/1471-2105-9-559

Le DT, Uram JN, Wang H, et al., 2015. Pd-1 blockade in tumors with mismatch-repair deficiency. N Engl J Med, 372(26):2509-2520. https://doi.org/10.1056/NEJMoa1500596

Le DT, Durham JN, Smith KN, et al., 2017. Mismatch repair deficiency predicts response of solid tumors to pd-1 blockade. Science, 357(6349):409-413. https://doi.org/10.1126/science.aan6733

Le DT, Kim TW, Van Cutsem E, et al., 2020. Phase ii open-label study of pembrolizumab in treatment-refractory, microsatellite instability-high/mismatch repair-deficient metastatic colorectal cancer: Keynote-164. J Clin Oncol, 38(1):11-19. https://doi.org/10.1200/JCO.19.02107

Lee HO, Hong Y, Etlioglu HE, et al., 2020. Lineage-dependent gene expression programs influence the immune landscape of colorectal cancer. Nat Genet, 52(6):594-603. https://doi.org/10.1038/s41588-020-0636-z

Li J, Qin S, Xu RH, et al., 2018. Effect of fruquintinib vs placebo on overall survival in patients with previously treated metastatic colorectal cancer: The fresco randomized clinical trial. JAMA, 319(24):2486-2496. https://doi.org/10.1001/jama.2018.7855

Li Y, Shen Z, Chai Z, et al., 2023. Targeting ms4a4a on tumour-associated macrophages restores cd8+ t-cell-mediated antitumour immunity. Gut, 72(12):2307-2320. https://doi.org/10.1136/gutjnl-2022-329147

Liebermeister W, Noor E, Flamholz A, et al., 2014. Visual account of protein investment in cellular functions. Proc Natl Acad Sci U S A, 111(23):8488-8493. https://doi.org/10.1073/pnas.1314810111

Mariathasan S, Turley SJ, Nickles D, et al., 2018. Tgfbeta attenuates tumour response to pd-l1 blockade by contributing to exclusion of t cells. Nature, 554(7693):544-548. https://doi.org/10.1038/nature25501

Mcdermott DF, Huseni MA, Atkins MB, et al., 2018. Clinical activity and molecular correlates of response to atezolizumab alone or in combination with bevacizumab versus sunitinib in renal cell carcinoma. Nat Med, 24(6):749-757. https://doi.org/10.1038/s41591-018-0053-3

Mints M, Landin D, Nasman A, et al., 2021. Tumour inflammation signature and expression of s100a12 and hla class i improve survival in hpv-negative hypopharyngeal cancer. Sci Rep, 11(1):1782. https://doi.org/10.1038/s41598-020-80226-z

Modest DP, Pant S, Sartore-Bianchi A, 2019. Treatment sequencing in metastatic colorectal cancer. Eur J Cancer, 109:70-83. https://doi.org/10.1016/j.ejca.2018.12.019

Overman MJ, Mcdermott R, Leach JL, et al., 2017. Nivolumab in patients with metastatic DNA mismatch repair-deficient or microsatellite instability-high colorectal cancer (checkmate 142): An open-label, multicentre, phase 2 study. Lancet Oncol, 18(9):1182-1191. https://doi.org/10.1016/S1470-2045(17)30422-9

Overman MJ, Lonardi S, Wong KYM, et al., 2018. Durable clinical benefit with nivolumab plus ipilimumab in DNA mismatch repair-deficient/microsatellite instability-high metastatic colorectal cancer. J Clin Oncol, 36(8):773-779. https://doi.org/10.1200/JCO.2017.76.9901

Parikh AR, Szabolcs A, Allen JN, et al., 2021. Radiation therapy enhances immunotherapy response in microsatellite stable colorectal and pancreatic adenocarcinoma in a phase ii trial. Nat Cancer, 2(11):1124-1135. https://doi.org/10.1038/s43018-021-00269-7

Qiu X, Mao Q, Tang Y, et al., 2017. Reversed graph embedding resolves complex single-cell trajectories. Nat Methods, 14(10):979-982. https://doi.org/10.1038/nmeth.4402

Rahma OE, Hodi FS, 2019. The intersection between tumor angiogenesis and immune suppression. Clin Cancer Res, 25(18):5449-5457. https://doi.org/10.1158/1078-0432.CCR-18-1543

Shi R, Wang X, Wu Y, et al., 2022. Apobec-mediated mutagenesis is a favorable predictor of prognosis and immunotherapy for bladder cancer patients: Evidence from pan-cancer analysis and multiple databases. Theranostics, 12(9):4181-4199. https://doi.org/10.7150/thno.73235

Socinski MA, Jotte RM, Cappuzzo F, et al., 2018. Atezolizumab for first-line treatment of metastatic nonsquamous nsclc. N Engl J Med, 378(24):2288-2301. https://doi.org/10.1056/NEJMoa1716948

Sung H, Ferlay J, Siegel RL, et al., 2021. Global cancer statistics 2020: Globocan estimates of incidence and mortality worldwide for 36 cancers in 185 countries. CA Cancer J Clin, 71(3):209-249. https://doi.org/10.3322/caac.21660

Wu Y, Yang S, Ma J, et al., 2022. Spatiotemporal immune landscape of colorectal cancer liver metastasis at single-cell level. Cancer Discov, 12(1):134-153. https://doi.org/10.1158/2159-8290.CD-21-0316

Zhang L, Yu X, Zheng L, et al., 2018. Lineage tracking reveals dynamic relationships of t cells in colorectal cancer. Nature, 564(7735):268-272. https://doi.org/10.1038/s41586-018-0694-x

Zhang L, Li Z, Skrzypczynska KM, et al., 2020. Single-cell analyses inform mechanisms of myeloid-targeted therapies in colon cancer. Cell, 181(2):442-459 e429. https://doi.org/10.1016/j.cell.2020.03.048

Zheng L, Qin S, Si W, et al., 2021. Pan-cancer single-cell landscape of tumor-infiltrating t cells. Science, 374(6574):abe6474. https://doi.org/10.1126/science.abe6474

Zheng RS, Zhang SW, Sun KX, et al., 2023. [cancer statistics in china, 2016]. Zhonghua Zhong Liu Za Zhi, 45(3):212-220. https://doi.org/10.3760/cma.j.cn112152-20220922-00647

Zhou H, Zhu L, Song J, et al., 2022. Liquid biopsy at the frontier of detection, prognosis and progression monitoring in colorectal cancer. Mol Cancer, 21(1):86. https://doi.org/10.1186/s12943-022-01556-2

Supplementary information:

Table S1-S11; Figs. S1-S9; Materials and methods